Citation
Li, Z. and Chen, W. and Hao, H. and Khan, M.Z.N. and Pham, T.M. 2021. Dynamic compressive properties of novel lightweight ambient-cured EPS geopolymer composite. Construction and Building Materials. 273: ARTN 122044.
http://doi.org/10.1016/j.conbuildmat.2020.122044

Dynamic compressive properties of novel lightweight ambient-cured EPS geopolymer composite

Zhixing Li[a], Wensu Chen[a]*, Hong Hao[a]*, Musaad Zaheer Nazir Khan[b], Thong M. Pham[a]

[a]Centre for Infrastructural Monitoring and Protection, School of Civil and Mechanical Engineering, Curtin University, Australia
[b]NUST Institute of Civil Engineering, School of Civil and Environmnetal Engineering, National University of Sciences and Technology, Pakistan
**Corresponding Authors: wensu.chen@curtin.edu.au (W. Chen), hong.hao@curtin.edu.au (H. Hao).*

Abstract

Geopolymer as eco-friendly and alternative cementitious material has been intensively investigated. In a previous study, Expanded Polystyrene (EPS) of volume fractions of 10%, 20% and 30% was mixed into the ambient-cured plain geopolymer mortar (GM) to form lightweight geopolymer composite (LGC). The static mechanical properties were tested and reported. The developed LGC can be used in various applications such as road barriers, tunnel cushions and lightweight building products i.e. bricks and panels, which could be subjected to dynamic loads such as impact or blast. Therefore, its dynamic properties need to be investigated. In this study, dynamic compressive properties of LGC were investigated by using Ø100-mm split Hopkinson pressure bar (SHPB). The failure processes and the failure modes of plain GM and LGC specimens with various EPS contents under different strain rates, as well as the stress-strain curves and the energy absorption capacity were compared. The strain rate effect on the dynamic compressive strength, axial strain at peak stress and normalized energy absorption capacities were compared and analysed. The test results showed that dynamic compressive properties and energy absorption capacity of LGC with more EPS contents

were more sensitive to the strain rate. Based on the testing results, the empirical formulae of dynamic increase factor of compressive strength and energy absorption versus strain rate were proposed.

Keywords: Expanded polystyrene; Lightweight geopolymer composite; SHPB; Impact loading; Strain rate effect; Energy absorption.

1. Introduction

Ordinary Portland Cement (OPC) has been widely used as the primary cementitious material, and its production keeps increasing by 9% annually around the world [1, 2]. Massive carbon dioxide (CO_2) can be released by calcining non-renewable natural resources, i.e. limestone and clay during cement production, which is an average of 6% of the total emissions around the world [3]. Therefore, the sustainable development of a new material to replace OPC has become increasingly important due to the greenhouse effect caused by CO_2. Geopolymer can be used as an alternative eco-friendly material to reduce resource and energy consumption as well as waste emissions [4]. Solid aluminosilicate sources can be activated by alkaline solutions to obtain geopolymer [5]. For instance, industrial waste or by-product materials from plants, i.e. fly ash (FA) and blast furnace slag as supplementary cementing materials were used in the manufacture of geopolymer. With the use of industrial wastes or by-products, geopolymer can reduce greenhouse gas emissions up to 80% [2].

Lightweight concrete (LWC) can be produced for various applications, such as load-bearing hollow bricks, cladding panels, slabs and reinforced concrete beams [6-9]. Depending on the requirements for various construction applications, lightweight aggregates could be incorporated in LWC either by partially or totally replacing natural aggregates. Expanded polystyrene (EPS) as an artificial material has been widely used in lightweight packaging, energy absorption and insulation applications [10-12]. It is worth noting that waste EPS has resulted in environmental issues. EPS with the density of 10~30 kg/m^3 has non-absorbent, hydrophobic and closed-cell nature. In recent years, numerous studies have been conducted to investigate the mechanical properties of LWC with EPS under the quasi-static or low-velocity impact [8, 13-19]. In the previous very limit studies, dynamic mechanical behaviours of LWC with EPS under high strain rates have been investigated. For example, Bai, et al. [20] used a split Hopkinson pressure bar apparatus (SHPB) to conduct dynamic compressive tests on LWC with different volume contents of EPS. As reported, the dynamic compressive strength of LWC with EPS exhibited strong sensitivity to the strain rate. This is because LWC is a heterogeneous material with different components, i.e., cement, aggregates and EPS, and likely the micro-cracks and air voids in the material, and these components, as well as their interfaces, have different mechanical properties. Under quasi-static or lower strain rate loading, cracks initiate and propagate along the relatively weaker sections in the specimen, therefore less cracks are developed and specimen fails with a few dominant fragments. When strain rate is high, cracks propagate quickly therefore have no time to seek weaker sections in the specimen. Specimen breaks into many number of small fragments. This different damage mode under dynamic loading contributes to the strain rate effect on the dynamic material properties. Other factors including viscosity, resistance from air and water trapped in the voids of the specimen, as well as inertial resistance also contribute to the dynamic material strength increment. In addition, it was found that EPS concrete was effective to improve the energy absorption capacity [21, 22]. Furthermore, the dynamic performance of a newly designed concrete barrier made of LWC with different EPS contents was investigated, and good energy absorption capacity was observed [23].

Geopolymer as an eco-friendly material has the potential to replace OPC, which has reasonable strength and sound physical properties, i.e. low water permeability, efficient thermal stability and low shrinkage [24-27]. Lightweight geopolymer concrete (LGC) as a novel lightweight material is developed by replacing OPC with geopolymer as matrix. LGC can be used in various applications such as road barriers, tunnel cushions and lightweight building products, i.e. bricks and panels, which could be subjected to dynamic loads such as impact or blast. Therefore, dynamic properties of LGC need to be investigated to understand the dynamic performance and energy absorption capacity of structures made of LGC. Currently, some studies have investigated the manufacturing process of heat-cured LGC with different volume fractions of EPS and the effect of EPS on the thermal and mechanical properties [28-31]. It was reported that the replacement of natural aggregates by EPS significantly improved the thermal insulation, but it led to a reduction of the compressive strength. Aslani, et al. [32] recently developed ambient-cured LGC with chemical treated EPS which used viscosity modifying agent as an admixture and obtained LGC with the compressive strength of 7.70~25.40 MPa and density of 1750 ~ 2200 kg/m^3. It is evident that these studies have mainly focused on the quasi-static material properties of ambient-cured or heat-cured LGC with EPS. To the best of authors' knowledge, no study has been conducted to investigate the dynamic mechanical properties of ambient-cured LGC with EPS under high strain rates.

In a previous study [3], the authors also mixed a LGC with the ambient cured GM and EPS of different volume percentages. The quasi-static compressive tests of plain GM and LGC containing EPS beads with volume fractions of 10%, 20% and 30% were conducted. The performances of LGC with different EPS volume fractions were observed and discussed, and the corresponding mechanical properties were defined. The mixed LGC showed reasonable mechanical properties and some potential applications were identified in constructions where lightweight materials with acceptable strength are required. In this study, as an extension of the previous study [3], the dynamic material properties of the developed LGC were quantified for the design analysis of structures made of LGC. The dynamic compressive tests were carried out in this study by using Ø100-mm split Hopkinson pressure bar (SHPB) with the strain rates up to 173.22 s^{-1}. The effects of strain rate on the failure process, failure mode, dynamic strength, axial strain at peak stress and energy absorption capacity of plain GM and LGC specimens were compared and analysed. The formulae pertaining to the dynamic increase factor of compressive strength (CDIF) and the energy absorption capacity of plain GM and LGC containing different EPS volume fractions were derived accordingly.

2. Experimental program

2.1. Material

Low calcium FA, type F as per ASTM 618-19 [33], with the median particle size of 9.7 µm was sourced from Gladstone power station, Queensland, Australia. A construction-grade blast furnace slag with the median particle size of 11.5 µm was provided by BGC cement, Perth, Australia. The alkaline activator was the mixture of 8-M (Molarity = 8 mol/L) sodium hydroxide (NaOH) solution and D-grade sodium silicate (Na_2SiO_3) (Specific gravity = 1.53). Silica sand (fineness modulus = 2.77 and specific gravity = 2.65) was supplied by Hanson Construction Materials. The commercially available EPS beads (Specific gravity = 0.0135) with the nominal diameter of 5- mm were obtained from a local company. The chemical compositions of the aluminosilicate materials (i.e. FA and slag) determined by X-ray fluorescence analysis (XRF) and alkaline activator solutions are presented in Table 1.

Table 1. Chemical compositions (weight %) of fly ash, slag, Sodium silicate (Na_2SiO_3) and Sodium hydroxide solution (NaOH) [3].

Composition (wt.%)	SiO_2	Na_2O	H_2O	Al_2O_3	Fe_2O_3	CaO	MgO	TiO_2	MnO	P_2O_5	K_2O	SO_3	Others	LOI
Fly ash	51.10	0.77	-	25.56	12.48	4.30	1.45	1.32	0.15	0.88	0.70	0.25	0.46	0.57
Slag	32.50	0.27	-	13.56	0.85	41.20	5.10	0.49	0.25	0.03	0.35	3.20	1.12	1.11
Na_2SiO_3	29.40	14.70	55.90	-	-	-	-	-	-	-	-	-	-	-
NaOH	-	28.05	71.95	-	-	-	-	-	-	-	-	-	-	-

Note: LOI is loss on ignition.

2.2. Mix proportions

For completeness, the mix proportions of plain GM and LGC with different EPS volume fractions in the previous study [3] are presented in Table 2. A combination solution of D-grade Na_2SiO_3 and 8-M NaOH solutions at a ratio of 2.50 was used as the alkaline activator. Both plain GM and LGC specimens had an identical ratio of alkaline activator to binder (FA and slag) of 0.40. The sand to binder ratio of 1.60 was used for plain GM. Fine aggregates were replaced with EPS beads at 10%, 20% and 30% in volume. LGC specimens with EPS volume fractions of 10%, 20% and 30% were labelled as EPS-10, EPS-20 and EPS-30, respectively. The use of slag can prohibit the segregation of EPS beads in the matrix and result in a reduction of the flow rate of the geopolymer matrix [34]. Therefore, the FA to slag ratio was maintained as 5.60 to obtain reasonable workability with uniform distribution of EPS beads for all mixtures (as shown in Fig. 1). More details about mixing, workability and curing of specimens can be found in [3].

Table 2. Mix proportions and flow rate of plain GM and LGC with different EPS contents [3].

Mix ID	Mix proportions (kg/m^3)					EPS beads		Flow rate
	Fly ash	Slag	NaOH	Na_2SiO_3	Sand	Wt. (kg/m^3)	Vol (%)	(%)
Plain GM	595	105	80	200	1120	-	-	104.33
EPS-10	595	105	80	200	855	1.35	10%	98.64
EPS-20	595	105	80	200	590	2.70	20%	80.27

EPS-30	595	105	80	200	325	4.05	30%	60.19

The sand of 10%, 20% and 30% in volume corresponding to 12.62%, 25.24% and 37.86% in weight was replaced with the EPS beads of 10%, 20% and 30% in volume. As calculated, the corresponding weight of sand proportion is 855 kg/m^3, 590 kg/m^3 and 325 kg/m^3 and that of EPS beads proportion is 1.35 kg/m^3, 2.70 kg/m^3 and 4.05 kg/m^3 for EPS-10, EPS-20 and EPS-30 mixtures, respectively.

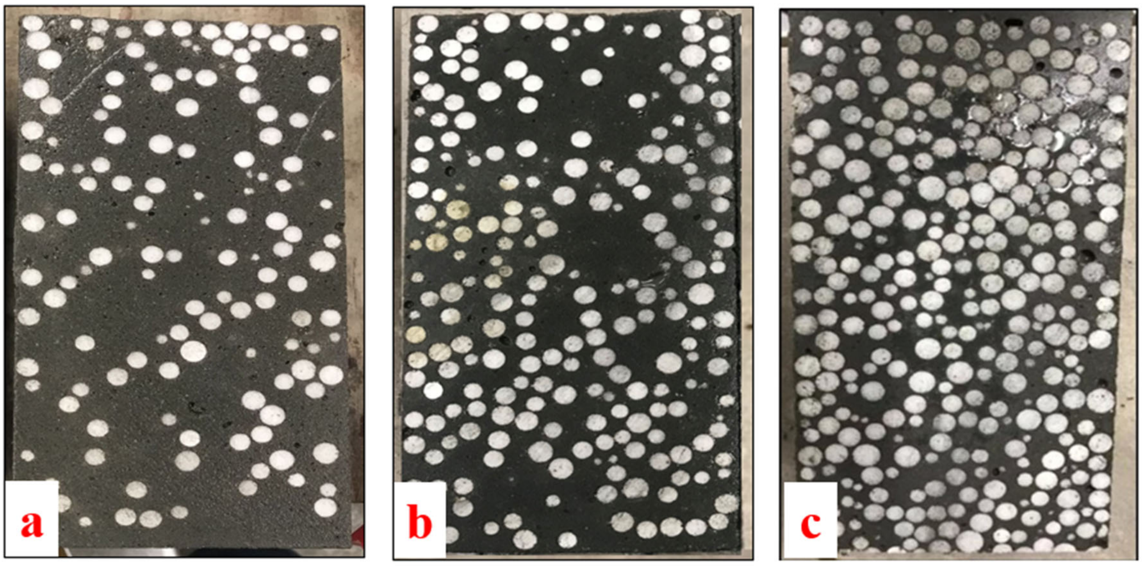

Fig. 1. Cross-sectional views of specimens. (a) EPS-10 specimen, (b) EPS-20 specimen, (c) EPS-30 specimen.

2.3. Experimental methodology

The SHPB test system was used to conduct the dynamic compressive tests in this study. A total of 51 specimens with a dimension of Ø100 × 50 mm, i.e. L/D =0.5 were prepared by cutting cylindrical specimens to disc. Both cut surfaces of the specimens were ground with surface roughness less than 0.02 mm. To quantify the dynamic strength increment and compare the failure modes of the specimens corresponding to different strain rates, the quasi-static tests and the results obtained in [3] are also briefly presented herein for easy reference.

2.3.1. Quasi-static test and results

The density of plain GM and LGC specimens was calculated as per ASTM C1688-14 [35]. The average value of the three specimens was obtained for each configuration. Quasi-static compressive tests were conducted as per ASTM C39-18 [36]. At least three sulfur-capped cylindrical specimens for each configuration were tested under a loading rate of 0.33 MPa/min with the strain rate of 1×10^{-4} s^{-1}. Modulus of elasticity (E) and Poisson's ratio (μ) were determined according to ASTM C469-14 [37].

Table 3. Quasi-static test results [3].

Mix ID	Density ρ^a (kg/m^3)	Compressive strength f_c^a (MPa)	Failure strain ε^a (%)	Modulus of elasticity E^a (GPa)	Poisson's ratio μ^a
Plain GM	2204.41	61.12	0.36	16.74	0.10
EPS-10	1791.86	24.33	0.25	9.66	0.13
EPS-20	1634.67	16.31	0.22	7.38	0.15
EPS-30	1284.31	6.32	0.13	4.83	0.19

Note: [a] presents 28-days mean value.

Table 3 gives the quasi-static results of plain GM and LGC with different EPS contents, which have been reported in [3] and are also presented herein as reference to obtain dynamic increase factor of compressive properties. The density of plain GM was 2204.41 kg/m^3, while that of EPS-10, EPS-20 and EPS-30 were 1791.86 kg/m^3, 1634.67 kg/m^3 and 1284.31 kg/m^3, respectively. The quasi-static strength and failure strain of LGC reduced with the increase of EPS contents due to the matrix replaced by the EPS beads with ultra-low density. The average compressive strengths of plain GM, EPS-10, EPS-20 and EPS-30 were 61.12 MPa, 24.33 MPa, 16.31 MPa and 6.32 MPa with the standard deviation of 1.43, 2.99, 1.98 and 0.39, respectively, and the average failure strains of plain

GM, EPS-10, EPS-20 and EPS-30 were 0.36%, 0.25%, 0.22% and 0.13% with the standard deviation of 0.04, 0.03, 0.06 and 0.02, respectively.

2.3.2. Dynamic compressive test procedure and equipment details

Dynamic compressive tests were conducted by using Ø100-mm SHPB test system. Dynamic properties of plain GM and LGC with different EPS contents including failure processes, failure patterns, dynamic compressive strengths, axial strain at peak stress and energy absorption capacities were carried out from the SHPB test. Fig. 2 shows that the SHPB system consists of three Ø100-mm pressure bars, including an incident bar with a length of 5500 mm, a transmitted bar with a length of 3000 mm and an absorption bar with a length of 1000 mm. The pressure bars were made of stainless steels with density, Young's modulus, elastic wave velocity and Poisson's ratio of 7800 kg/m^3, 240 GPa, 5064 m/s and 0.30, respectively. A striker bar with a length of 400 mm was made of the same material as the pressure bars. The signal was recorded by two strain gauges at the middle of both incident and transmitted bars. The failure process of plain GM and LGC specimens were recorded by using a high-speed camera. Before the impact tests, grease was applied to interfaces between the specimen and pressure bars to minimize the effect of end friction confinement. As shown in Fig. 3, an Ø20-mm circular rubber pulse shaper with a thickness of 3 mm was attached to the impact end of the incident bar. At least three specimens were tested under the same impact load for each configuration.

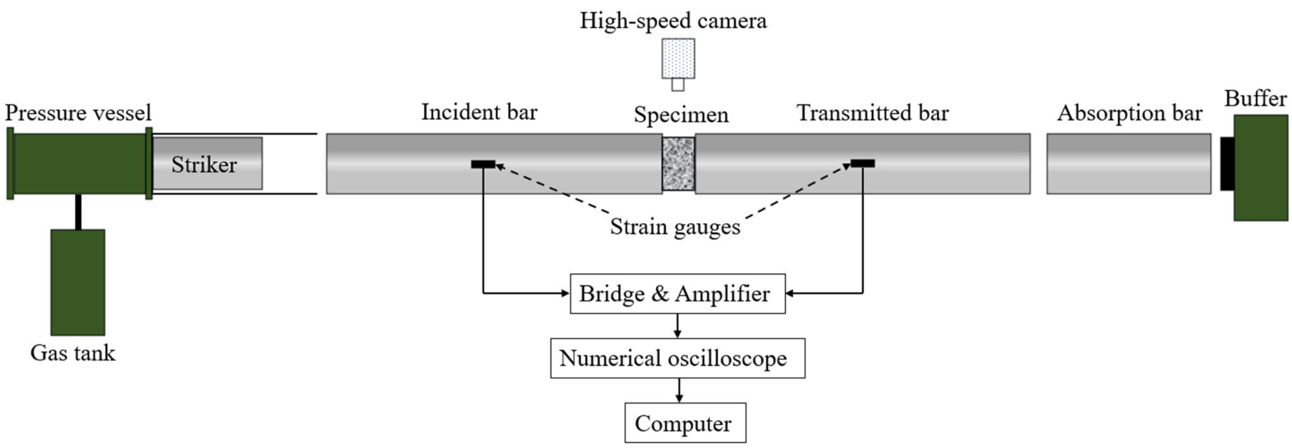

(a)

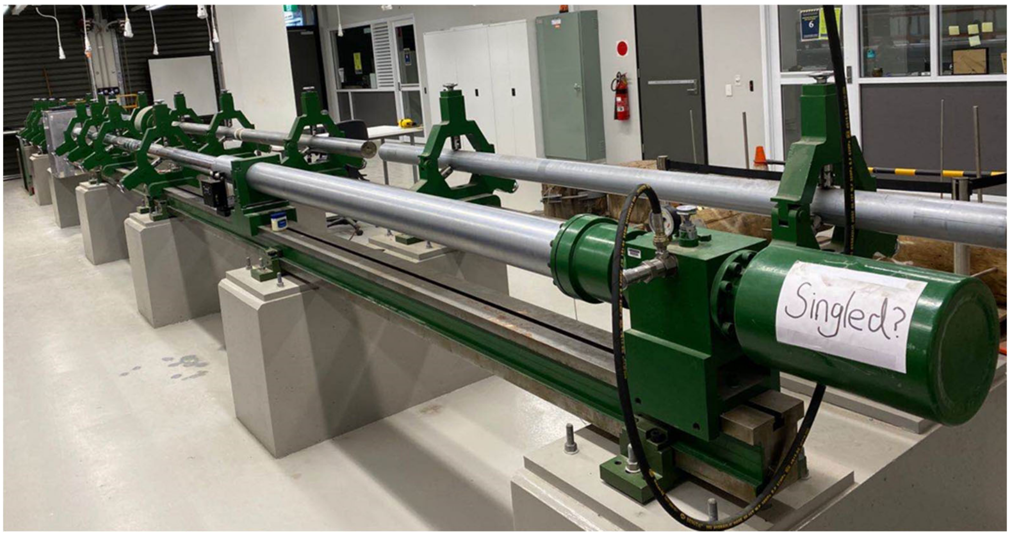

(b)

Fig. 2. (a) Schematic and (b) actual set-up of SHPB system.

Fig. 3. Rubber pulse shaper.

3. Dynamic test results and discussions

3.1. Validity and strain rate determination of SHPB tests

Fig. 4 shows typical stress wave signals recorded in the incident and transmitter bars. The incident wave was shaped with the aid of rubber pulse shaper in the test. The pulse shaper can not only mitigate the high frequency oscillation at the front of the incident wave but also extend the rising time of the incident pulse, which can facilitate achieving the dynamic stress equilibrium in the specimen [38].

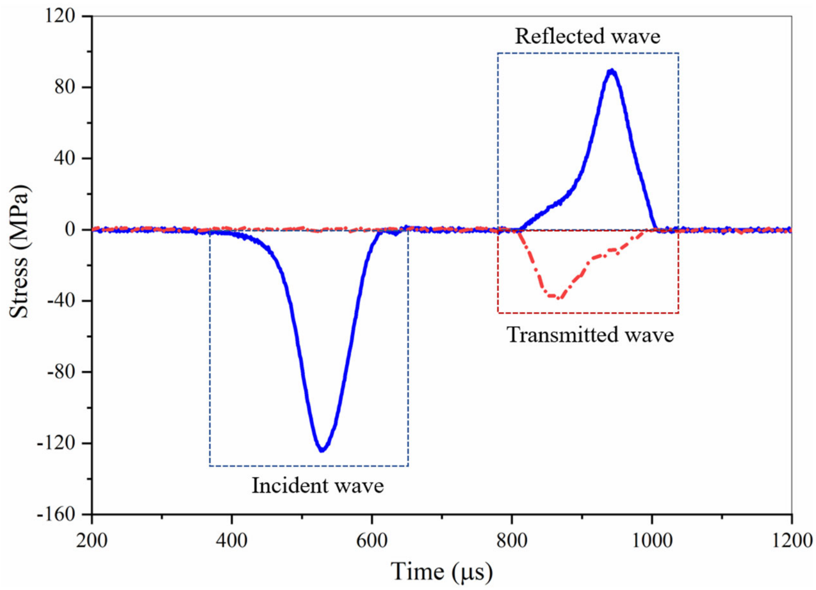

Fig. 4. Typical stress wave signals recorded in the incident and transmitter bars.

Dynamic compressive properties of the specimens were derived from the recorded data. One-dimensional wave propagation theory was applied. It should be noted that the data is valid only when the specimen achieved dynamic stress equilibrium. The stress (σ), strain rate ($\dot{\varepsilon}$) and strain (ε) of the specimens can be calculated by the equations below, respectively [39].

$$\sigma(t) = E_b(\frac{A_b}{A_s})\varepsilon_T(t) \quad (1)$$

$$\dot{\varepsilon}(t) = \frac{2C_0}{L}\varepsilon_R(t) \quad (2)$$

$$\varepsilon(t) = \int_0^T \dot{\varepsilon}\,(t)dt \quad (3)$$

where E_b, A_b and C_0 are the modulus of elasticity, cross-section area and elastic wave velocity of the pressure bars, respectively; A_s and L are the cross-section area and length of the tested specimen, respectively; ε_T and ε_R are the recorded time-dependent transmitted and reflected strain.

Fig. 5 shows the typical dynamic stress equilibrium of SHPB test, which was checked for all test results. Fig. 6 (a)-(d) demonstrate the stress equilibrium status of plain GM and LGC with different EPS contents at strain rate of around 150 s^{-1}, indicating the validity of dynamic compressive test results in this study.

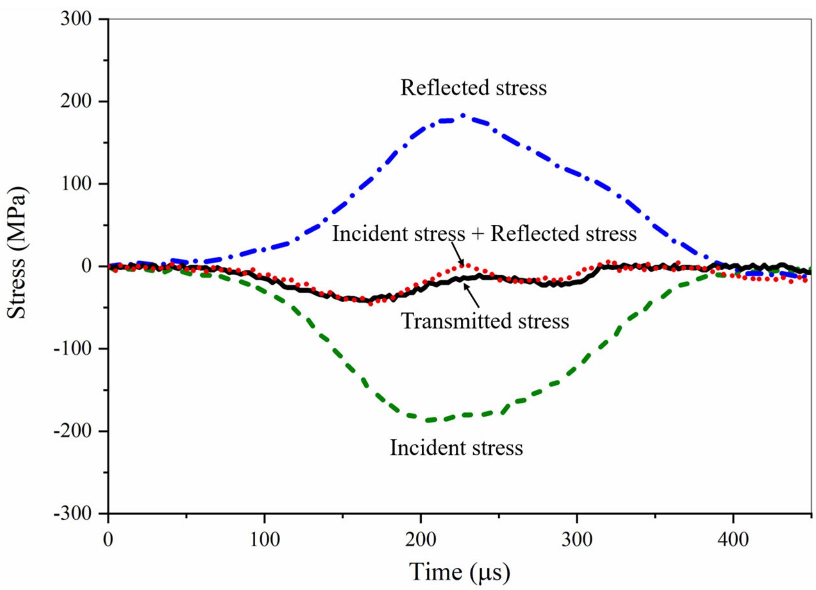

Fig. 5. Typical stress equilibrium of SHPB test.

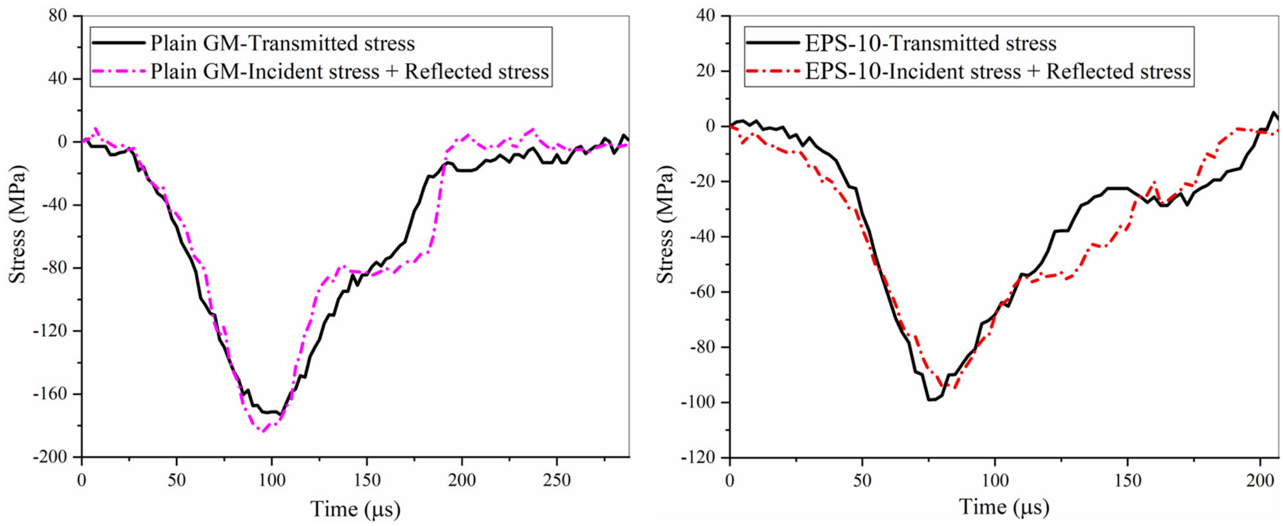

(a) (b)

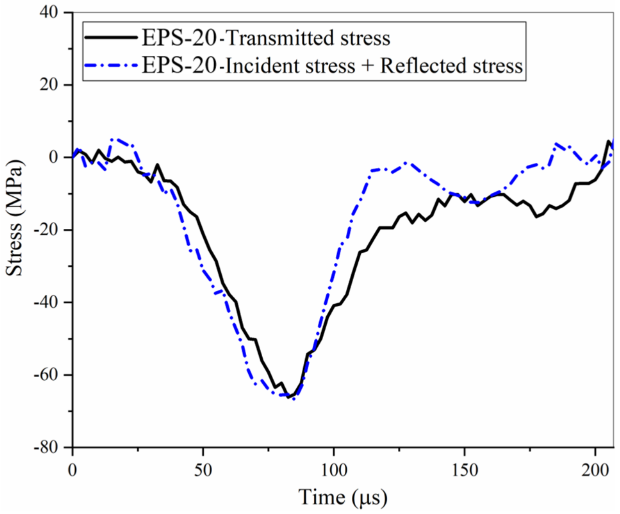

(c)

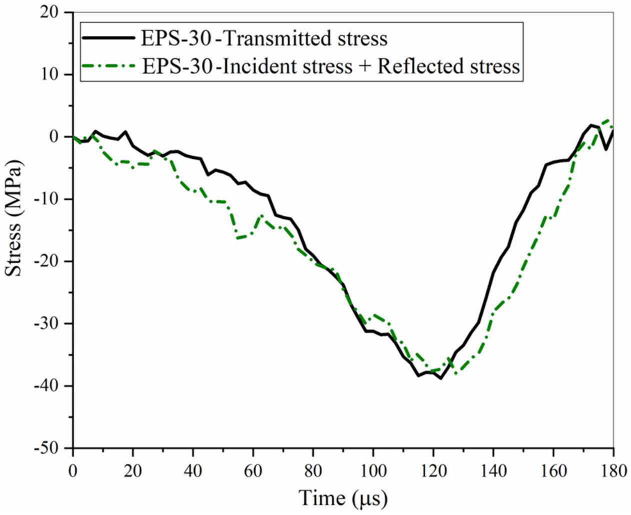

(d)

Fig. 6. Typical stress equilibrium of (a) Plain GM specimen, (b) EPS-10 specimen, (c) EPS-20 Specimen, (d) EPS-30 specimen.

According to Eq.(3), the strain rate is determined by the reflected signal. There are several methods to determine the representative strain rate from results in the SHPB test. As reported in [40, 41], the mean value of the strain rate during the loading period was used as the representative strain rate. In addition, the strain rate can be represented by the strain rate at the failure point [42]. A nearly constant strain rate as the representative strain rate has been used as well [43-45]. In this study, the value corresponding to the maximum compressive stress was taken as the strain rate of the tested specimen as shown in Fig. 7, which has been also used to determine the strain rate of concrete-like material in SHPB test in the previous studies [42, 46, 47].

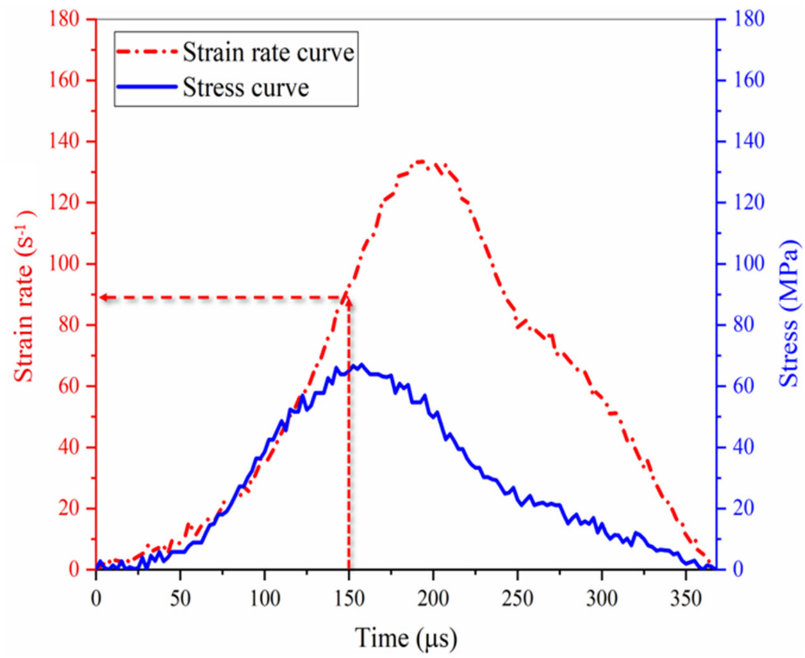

Fig. 7. Strain rate determination.

3.2. Failure process and failure mode

The failure process was recorded by using a high-speed camera with 40,000 frames per second (fps) and a resolution of 640 × 744 pixels. Fig. 8 (a)-(d) show the failure process of plain GM and LGC with different EPS contents at strain rate of around 150 s^{-1}. The first image corresponded to the instant when the specimens were initially stressed. For plain GM, surface cracks were initiated from both edges of the specimen at around 150 μs, which extended further to the mid region. The specimen was shattered into small pieces at around 400 μs.

For LGC, surface cracks were initiated earlier than that of plain GM because of lower compressive strength and porous structures of LGC. In addition, the time of surface cracks initiation of LGC specimens was delayed with the increase of EPS volume content from 10% to 30% at a similar strain rate. As observed, surface cracks in the specimens EPS-10, EPS-20 and EPS-30 initiated at around 80, 100 and 125 μs, and then pulverized at around 250 μs. It might be due to the enhanced deformation ability of LGC specimen with the increase of EPS volume fraction.

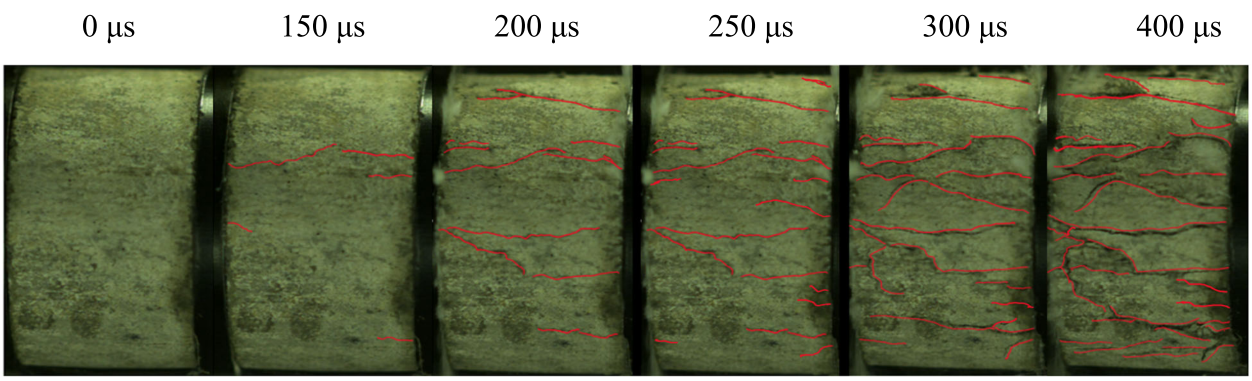

(a) Plain GM specimen

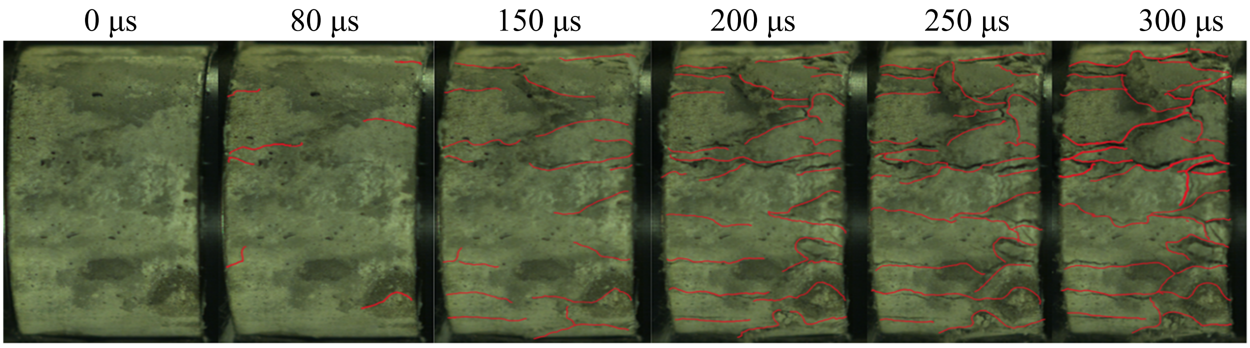

(b) EPS-10 specimen

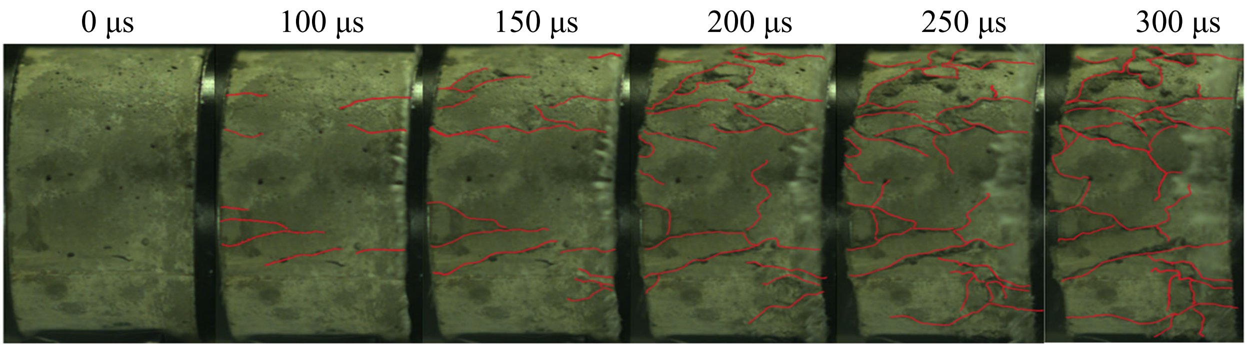

(c) EPS-20 specimen

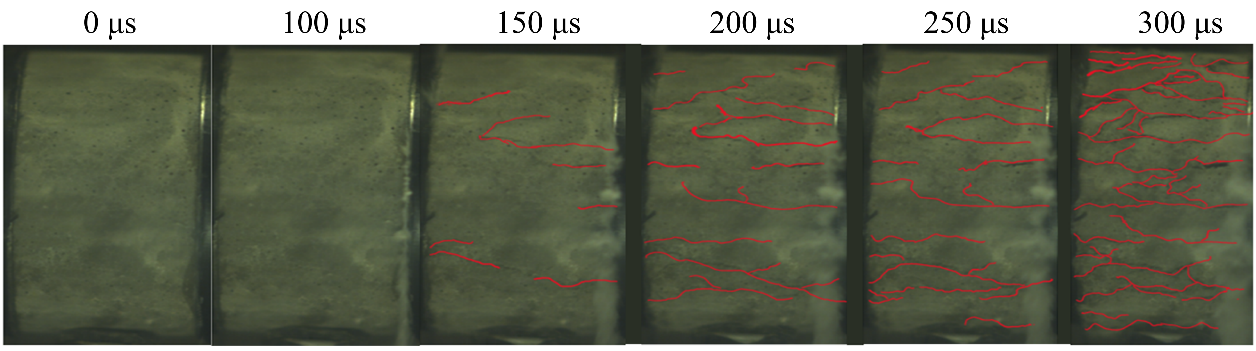

(d) EPS-30 specimen

Fig. 8. Fracture images and failure process of the specimens at strain rate of around 150 s^{-1}.

Failure patterns of plain GM and LGC with different EPS volume fractions are shown in Fig. 9 (a)-(d). As observed, the rising strain rate significantly affected the failure modes of plain GM and LGC. The damage levels of plain GM and LGC specimens became more severe with the higher strain rates, and the average size of fragments of test specimens decreased. As shown in Fig. 9(a), the specimens of plain GM experienced edge cracks at strain rate of 65.76 s^{-1}. Then, the specimen failed with many numbers of fragments, and the number of fragments increased, and the size of the average fragments decreased with the increase of the strain rates. At strain rate of 173.22 s^{-1}, the test specimen was shattered into smaller fragments.

The effect of the high strain rate on the failure patterns can be explained by the strain-rate hardening effect, which demonstrates that the compressive strength and energy absorption capacities of test specimen increase with the rising strain rate [48]. Firstly, when the specimen is under quasi-static compression, the plain GM specimen failed in a sudden manner [3]. It is considered that micro-cracks and tiny voids were produced due to slurry shrinkage and local compression of the matrix during the casting and curing process. With the rising strain rate, the specimen failed due to both newly generated cracks and the spread of existing cracks. It was reported that more energy was required to produce new cracks than that required for the spread of existing cracks [21]. Therefore, with the rising strain rate, the developed number of cracks and the required amount of energy increased during this process. Consequently, more fragments with smaller size were expanded from the internal cracks of plain GM specimens.

For the specimens of LGC with different EPS contents, the damage level was severer with the increase of EPS volume fractions under a similar strain rate. As shown in Fig. 9 (b)-(c), with the rising strain rate, the specimen of EPS-10 experienced four damage levels, i.e. partially crush, crush into pieces and pulverize into small fragments, which indicated more energy absorption at higher strain rate. The failure mode of EPS-20 had similar trends that the specimen was shattered into smaller fragments with the rising strain rate. It should be noted that EPS-30 was broken but kept its structural integrity at strain rate of 51.12 s^{-1} and then pulverized into smaller pieces with the rising strain rate. The failure mode of LGC with the rising strain rate is consistent with the previous studies of LWC with EPS [21].

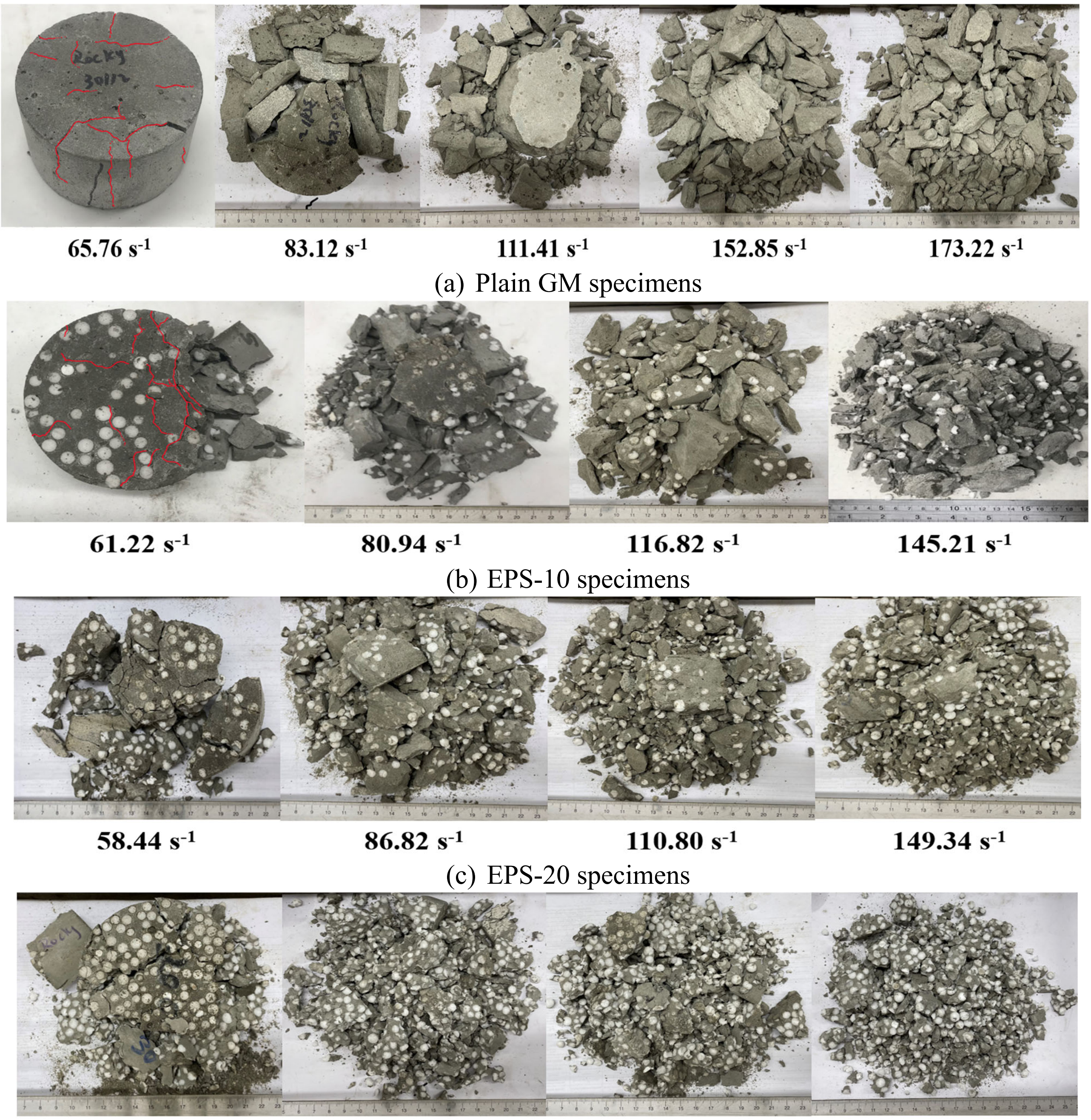

65.76 s^{-1} **83.12 s^{-1}** **111.41 s^{-1}** **152.85 s^{-1}** **173.22 s^{-1}**

(a) Plain GM specimens

61.22 s^{-1} **80.94 s^{-1}** **116.82 s^{-1}** **145.21 s^{-1}**

(b) EPS-10 specimens

58.44 s^{-1} **86.82 s^{-1}** **110.80 s^{-1}** **149.34 s^{-1}**

(c) EPS-20 specimens

51.12 s^{-1} **74.29 s^{-1}** **112.76 s^{-1}** **144.31 s^{-1}**

(d) EPS-30 specimens

Fig. 9. Failure patterns of specimens under high strain rates.

3.3. Dynamic stress-strain curves

Fig. 10 (a)-(d) show the dynamic compressive stress-strain curves of plain GM and LGC with different EPS volume fractions at different strain rates. As shown, the compressive strength of all specimens increased with the rising strain rate, i.e. the dynamic compressive strength of plain GM increased from 82.84 MPa at strain rate of 65.76 s^{-1} to 191.02 MPa at strain rate of 173.22 s^{-1}, and the strength of EPS-10 increased from 50.56 MPa at strain rate of 61.22 s^{-1} to 97.22 MPa at strain rate of 145.21 s^{-1}. Fig. 10 (c) and (d) show that the dynamic compressive strength of EPS-20 increased from 38.38 MPa at strain rate of 58.44 s^{-1} to 71.18 MPa at strain rate of 149.34 s^{-1} and the dynamic compressive strength of EPS-30 increased from 23.37 MPa at strain rate of 51.12 s^{-1} to 37.18 MPa at strain rate of 144.31 s^{-1}. It means that the compressive strength of plain GM and LGC was sensitive to the strain rate, which is consistent with the previous studies about strain rate effect on the compressive strength under impact loadings [21, 48]. It is due to the strain-rate hardening effect as explained in section 3.2, which indicates that more external energy and impulse can be absorbed by the production and spread of internal cracks owing to the theory of work-energy and impulse-momentum. As a result, the rising strain rate can lead to the higher compressive strength of the test specimen under impact loadings.

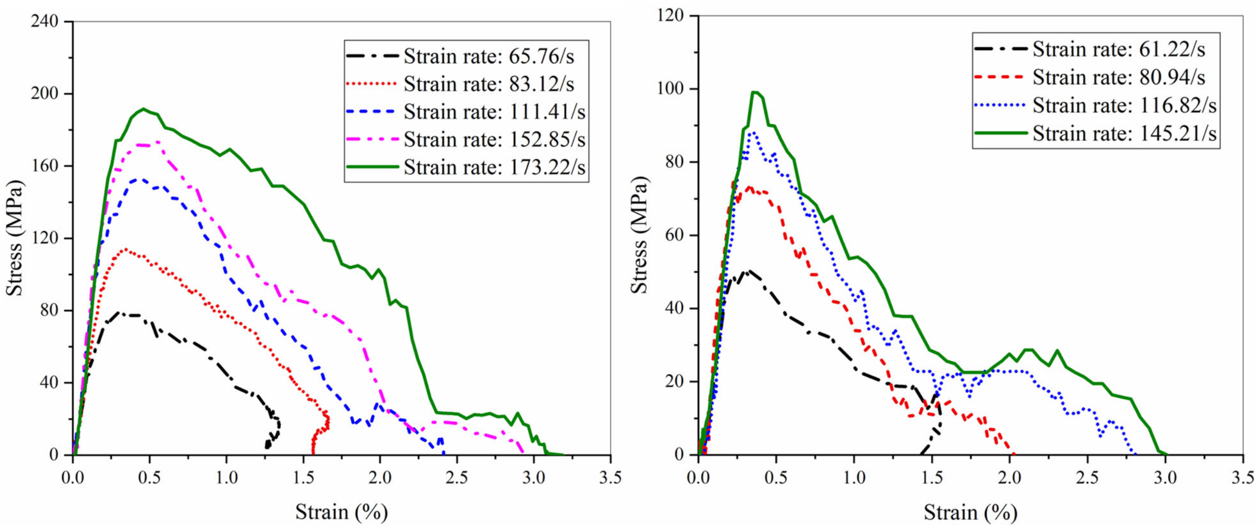

(a) Plain GM (b) EPS-10

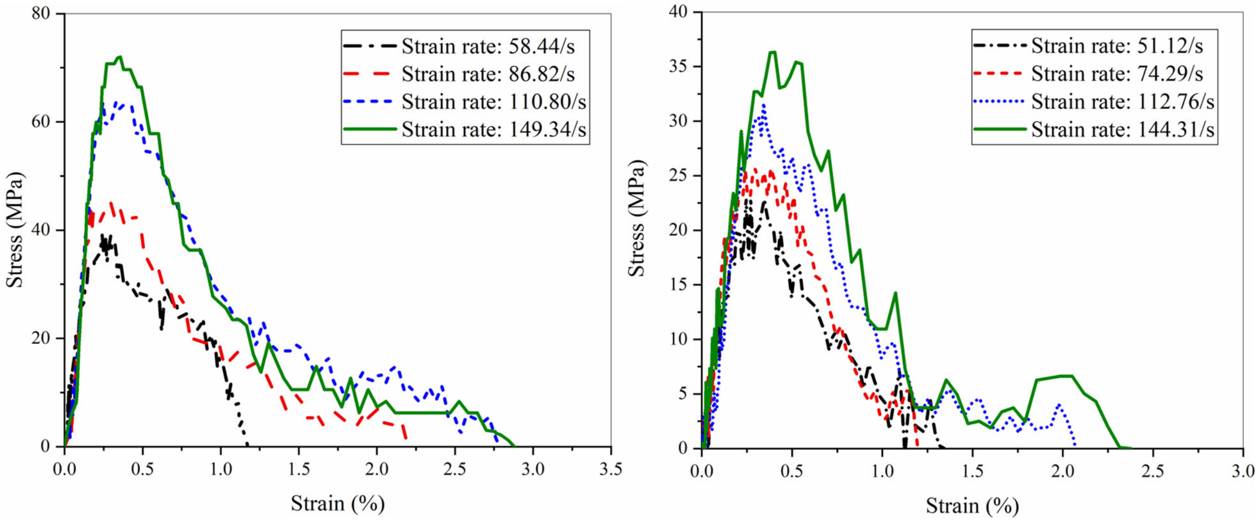

(c) EPS-20 (d) EPS-30

Fig. 10. Comparison of dynamic stress–strain curves.

3.4. Rate effects on dynamic properties

Strain rate effect on the compressive strength of concrete-like materials under impact loadings is commonly quantified by the dynamic increase factor (CDIF), which is derived by normalizing the dynamic compressive strength by the quasi-static compressive strength. According to Eq. (1), the dynamic compressive strength can be determined by the peak stress. It should be noted that the dynamic compressive strength is also affected by the lateral inertial confinement and the end friction effects [49]. In this study, the effect of the end friction effect has been minimized by applying grease at the interfaces of the specimen and pressure bars. Meanwhile, the lateral inertial confinement as a structural effect always exists under high strain rates loading due to the Poisson's effect, which can enhance the load capacity of the specimen [44]. The contribution of lateral inertial confinement to the CDIF should be removed from the experimental results of CDIF ($CDIF_E$) to obtain the true CDIF ($CDIF_T$) of the specimen. The contribution of the lateral inertial confinement of different specimen sizes to CDIF was numerically quantified by the previous study [50], which is specimen size, mass density and strain rate dependent. For instance, the contribution of lateral inertial confinement of the

Ø100 specimen reached 13.68% at strain rate of 200 s^{-1}. The $CDIF_T$ of the specimen was obtained by removing the contribution of lateral inertial confinement effect according to the empirical relation proposed in [50].

Fig. 11 presents the strain-rate effect on the dynamic compressive strength of plain GM and LGC with various EPS contents. The $CDIF_T$ of plain GM and LGC increased with the rising strain rate, which was due to the strain-rate hardening effect. Additionally, the $CDIF_T$ of EPS-30 was the most sensitive to strain rate, followed by EPS-20, EPS-10 and then the plain GM, i.e. the $CDIF_T$ of EPS-30, EPS-20, EPS-10 and plain GM were 4.34, 3.51, 3.23 and 2.21 at strain rate around 110 s^{-1}, respectively. It is indicated that LGC with higher EPS volume fraction was more sensitive to the strain rate. It should be noted that LGC with EPS is a heterogeneous material with geopolymer mortar matrix, EPS beads, initial inherent micro-cracks, tiny voids and discontinuities. The internal pore of EPS beads was restrained due to the viscosity effect (as shown in Fig. 12), which increased the dynamic compressive strength under impact loadings. Besides, with the increase of EPS volume fraction, more inherent micro-cracks, tiny voids and discontinuities were more likely produced during the casting and curing process. Under the high strain rate, more cracks were generated from inherent micro-cracks, tiny voids and discontinuities inside the matrix. Consequently, the increase of EPS volume fraction resulted in the higher $CDIF_T$ at a similar strain rate in this study. Based on the test results, the predictions of $CDIF_T$ for plain GM and LGC at their corresponding strain rate ($\dot{\varepsilon}$) ranges, are given as:

For plain GM:

$$CDIF_T = 1.537\ln(\dot{\varepsilon}) - 5.187 \quad \text{for } 61.79\ \text{s}^{-1} < \dot{\varepsilon} < 173.22\ \text{s}^{-1}\ (R^2 = 0.961) \tag{4}$$

For EPS-10:

$$CDIF_T = 1.719\ln(\dot{\varepsilon}) - 5.073 \text{ for } 54.26 \text{ s}^{-1} < \dot{\varepsilon} < 152.92 \text{ s}^{-1} \ (R^2 = 0.965) \quad (5)$$

For EPS-20:

$$CDIF_T = 1.710\ln(\dot{\varepsilon}) - 4.771 \text{ for } 49.53 \text{ s}^{-1} < \dot{\varepsilon} < 149.34 \text{ s}^{-1} \ (R^2 = 0.924) \quad (6)$$

For EPS-30:

$$CDIF_T = 1.638\ln(\dot{\varepsilon}) - 3.046 \text{ for } 43.87 \text{ s}^{-1} < \dot{\varepsilon} < 149.33 \text{ s}^{-1} \ (R^2 = 0.928) \quad (7)$$

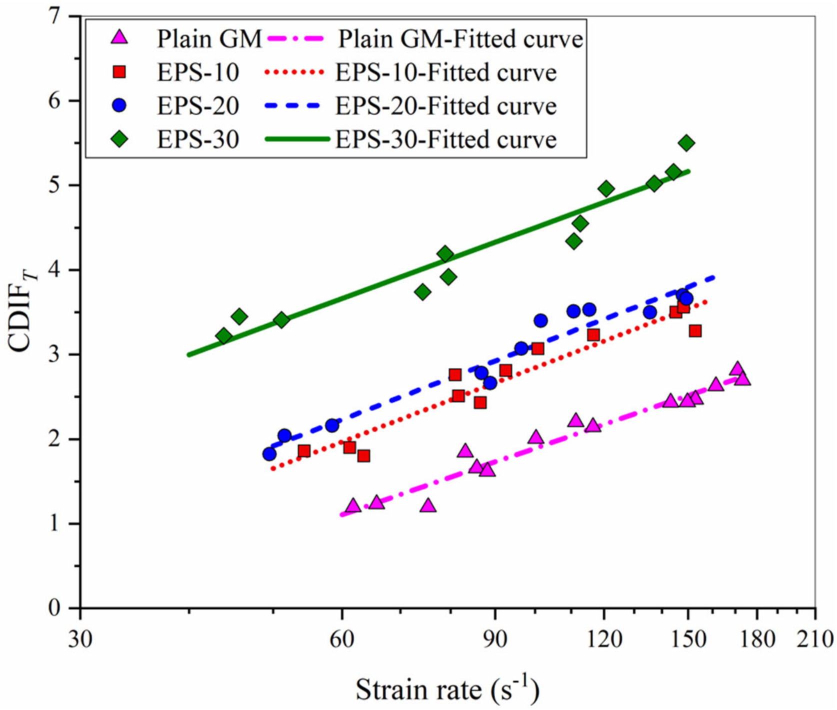

Fig. 11. Relationship between the CDIF$_T$ and strain rate.

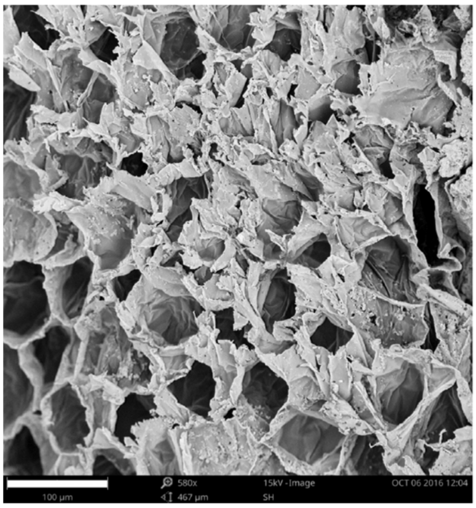

Fig. 12. Cell-structure of EPS bead [30].

Fig. 13 compares the test results from the previous studies on CDIF of plain GM [48, 51] and LWC with EPS [20, 52] with the test results in this study. As observed, the CDIF of plain GM in this study was more sensitive to the strain rate than the test results of GM reported by Khan, et al. [48] and Feng, et al. [51]. It is due to different mix proportions, the synthesis environment and curing conditions of GM, i.e. more slag (FA/slag =1.5) was used as ingredients to prepare ambient-cured GM specimens with compressive strength of 112 MPa in [48], while the heat-cured plain GM specimens with compressive strength of 68 MPa were prepared by using fly ash as ingredients [51]. As reported in [53], the ratio of ingredients and curing condition affected the microstructure, i.e. micro-cracks, tiny voids and discontinuities, or moisture condition within the specimen of GM, which can influence the dynamic behaviours at high strain rate.

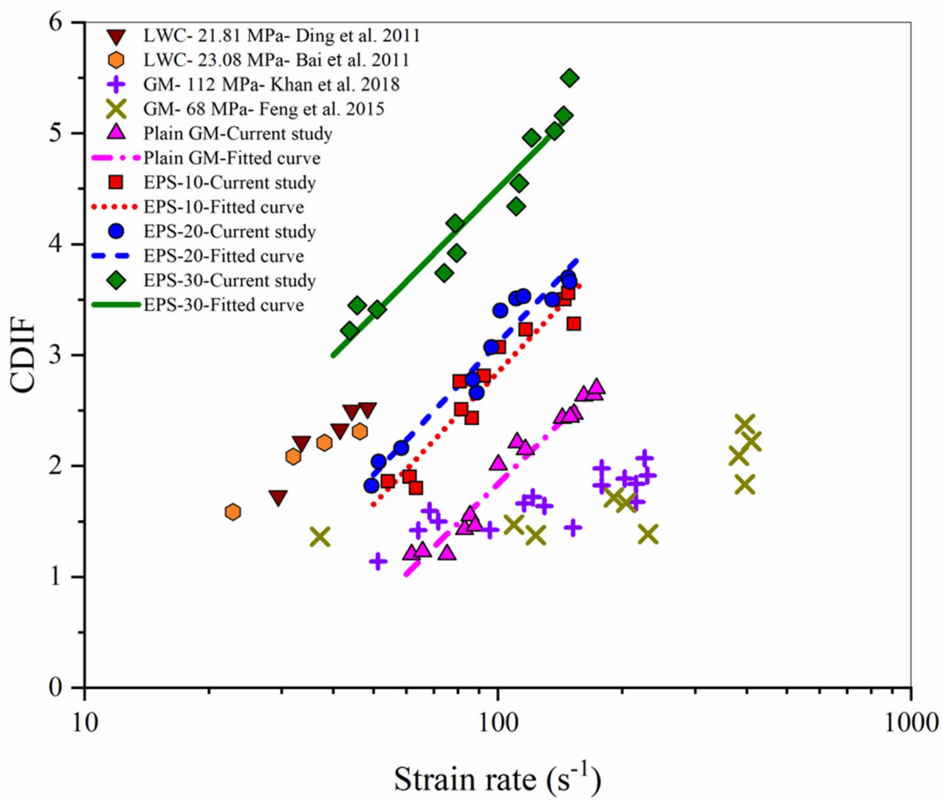

Fig. 13. Comparison of CDIF from this study and previous studies.

Furthermore, the test results of the previous studies on LWC with EPS are shown in Fig. 13. The CDIF of LGC with EPS specimens had similar trend as that of LWC with EPS specimens. As observed, the test results of LWC with EPS and partial coarse aggregates reported by Bai, et al. [20] and Ding, et al. [52] displayed a higher CDIF as compared with EPS-10 of similar compressive strength. It is because the regions with coarse aggregates of LWC experienced cleaving under high strain rates, which can obtain a higher compressive strength increase.

As observed in Fig. 10, the axial strain corresponding to peak stress of plain GM and LGC increased with the rising strain rate, i.e. the axial strain of plain GM was 0.39% at strain rate of 65.76 s^{-1} and increased to 0.45% at strain rate of 173.22 s^{-1}. The CDIF of axial strain ($CDIF_{\varepsilon}$) was normalized by the quasi-static failure strain to evaluate the strain rate effect on the strain at peak stress. Fig. 14 presents the strain rate effect on the axial strain of plain GM and LGC with various EPS contents. As observed, the axial strain of both plain GM and LGC was consistently enhanced with the rising strain rate. Meanwhile, the specimen of LGC with higher EPS contents were more sensitive to the higher strain rate, i.e. the $CDIF_{\varepsilon}$ of plain GM was 1.08 at strain rate of 65.76 s^{-1} and increased to 1.42 at strain rate of 152.85 s^{-1}, while $CDIF_{\varepsilon}$ of EPS-30 was 1.31 at strain rate of 51.12 s^{-1} and increased to 3.23 at strain rate of 144.31 s^{-1}. It may be due to the great deformation ability of EPS beads. It is worth noting that the increasing trend of strain at peak compressive stress of concrete-like material with the rising strain rate was reported in some previous studies [40, 46], while nearly constant axial strain [54] and a declining trend of axial strain with the rising strain rate [55, 56] were also reported. Therefore, further study regarding the strain rate effect on axial strain corresponding to peak stress of plain GM and LGC is necessary.

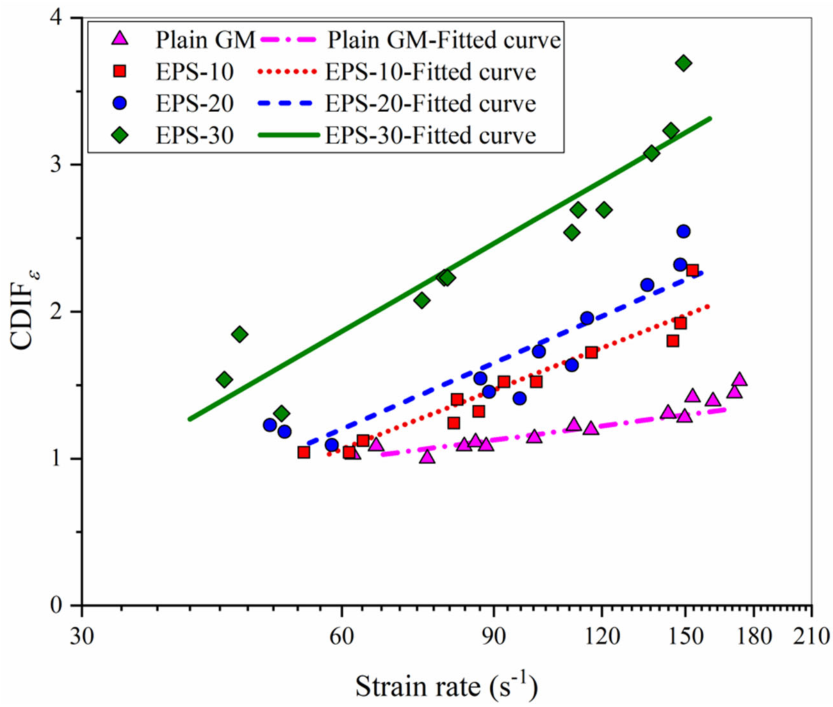

Fig. 14. Relationship between CDIF$_\varepsilon$ and strain rate.

3.5. Energy absorption

Energy absorption capacity can be evaluated by the Strain Energy Density (SED), which is determined by the combined effect of ductility and strength under high strain rates [49]. In order to demonstrate the effect of strain rate on energy absorption capability of plain GM and LGC with different EPS contents, Eq.(8) was used to calculate SED, which can be determined by the enclosed area of stress-strain curves as shown in Fig. 15.

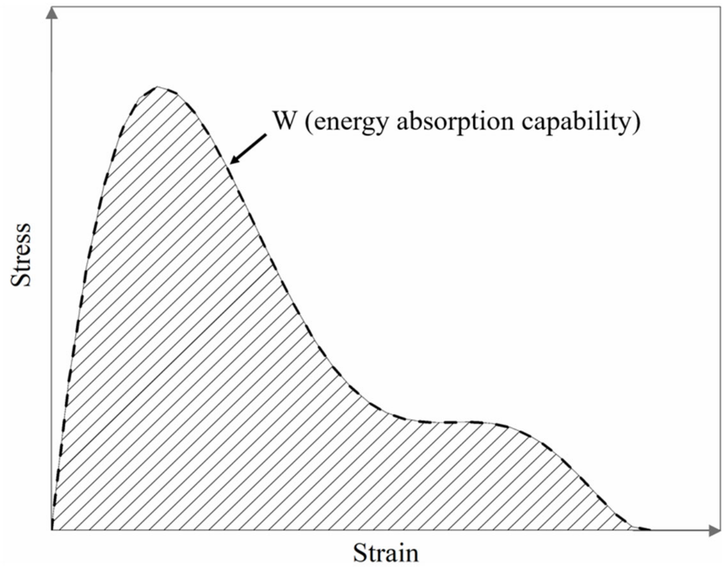

Fig. 15. Strain energy density of concrete-like material.

$$W = \int_0^T \sigma(t) d\varepsilon(t) \tag{8}$$

where W is the strain energy density, σ(t) denotes the time-dependent stress and ε(t) represents time dependent strain.

Fig. 16 shows the comparison of energy absorption capacities of plain GM and LGC. As shown, the SED of both plain GM and LGC with different EPS contents increased with the rising strain rate, i.e. the SED of plain GM increased from 711.90 KJ/m^3 at strain rate of 61.79 s^{-1} to 2960.42 KJ/m^3 at strain rate of 173.22 s^{-1}, and the SED of EPS-30 increased from 143.24 KJ/m^3 at strain rate of 45.72 s^{-1} to 350.95 KJ/m^3 at strain rate of 149.33 s^{-1}. Plain GM exhibited the highest SED due to the higher compressive strength although it had the lowest deformation ability. As observed, the energy absorption capacity of plain GM specimens is more strain rate dependent as compared with LGC specimens. It was reported that the energy absorption capacity as a synthesized index was determined by both strength and deformation ability of material [21]. As the EPS volume content increases, the reduction level of strength has more significant effect on the energy absorption capacity than the enhanced level of deformation ability, which resulted in the reduction of overall energy absorption performance of LGC.

The relationship between SED and strain rate ($\dot{\varepsilon}$) within their corresponding strain rate range can be expressed as:

For plain GM:

$$\mathrm{SED} = -0.083\dot{\varepsilon}^2 + 41.799\dot{\varepsilon} - 1627.00 \quad \text{for } 61.79\ \mathrm{s^{-1}} < \dot{\varepsilon} < 173.22\ \mathrm{s^{-1}}\ (R^2 = 0.951) \tag{9}$$

For EPS-10:

$$\mathrm{SED} = -0.0537\dot{\varepsilon}^2 + 21.085\dot{\varepsilon} - 626.96 \quad \text{for } 54.26\ \mathrm{s^{-1}} < \dot{\varepsilon} < 152.92\ \mathrm{s^{-1}}\ (R^2 = 0.9596) \tag{10}$$

For EPS-20:

$$\mathrm{SED} = -0.0098\dot{\varepsilon}^2 + 9.7239\dot{\varepsilon} - 206.37 \quad \text{for } 49.53\ \mathrm{s^{-1}} < \dot{\varepsilon} < 149.34\ \mathrm{s^{-1}}\ (R^2 = 0.9728) \tag{11}$$

For EPS-30:

$$\mathrm{SED} = 0.0103\dot{\varepsilon}^2 - 0.1443\dot{\varepsilon} + 147.75 \quad \text{for } 43.87\ \mathrm{s^{-1}} < \dot{\varepsilon} < 149.33\ \mathrm{s^{-1}}\ (R^2 = 0.9381) \tag{12}$$

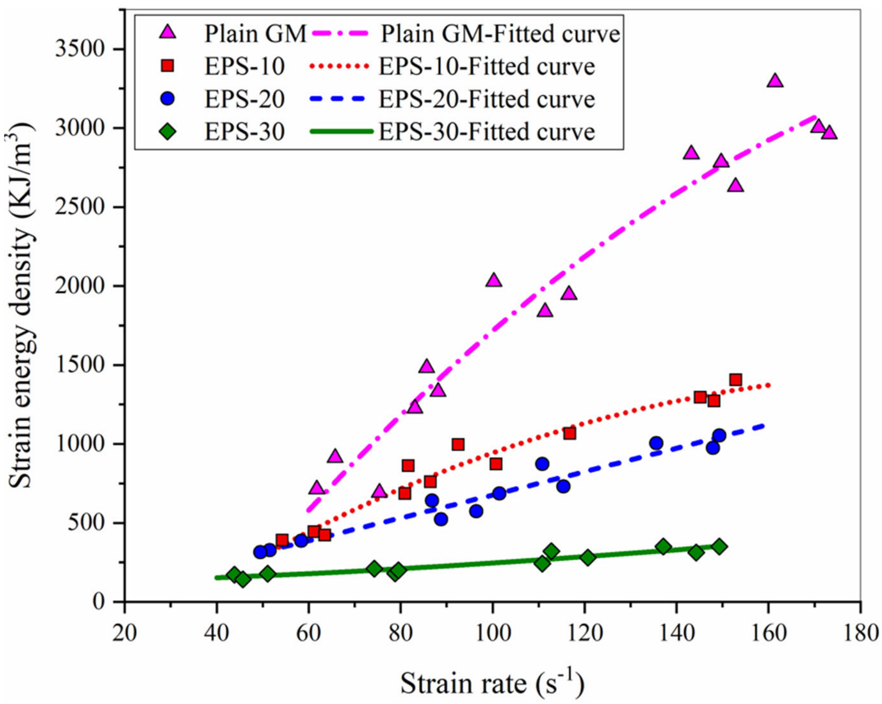

Fig. 16. Comparison of strain energy density (SED) of plain GM and LGC.

As observed, the energy absorption capacities of material were greatly influenced by the compressive strength. To evaluate the effect of EPS volume contents on the energy absorption capacities of LGC with various strengths, the specific energy absorption (SEA) capacity was normalized with quasi-static compressive strength [46]. Fig. 17 presents comparison of specific SEA of plain GM and LGC at different strain rates. As observed, the SEA of LGC was higher than that of plain GM, i.e. the SEA of plain GM was 45.54 KJ/m3/MPa at strain rate of 149.69 s-1, while that of EPS-30 was 55.53 KJ/m3/MPa at strain rate of 149.33 s-1. It is demonstrated that LGC with EPS can absorb more energy than plain GM of the same compressive strength. For LGC with different EPS contents, the SEA of EPS-20 was slightly higher than that of EPS-10 in general. It is interesting to observe that the SEA of EPS-30 was higher than that of EPS-20 at strain rate range from 40 s-1 to 80 s-1 but lower at strain rate range from 80 s-1 to 150 s-1, which was mainly because that the weak bonding between geopolymer matrix and EPS beads reduced the toughness of EPS-30 under higher strain rate. Dynamic compressive test results of all specimens are summarized in Table 4 - Table 7.

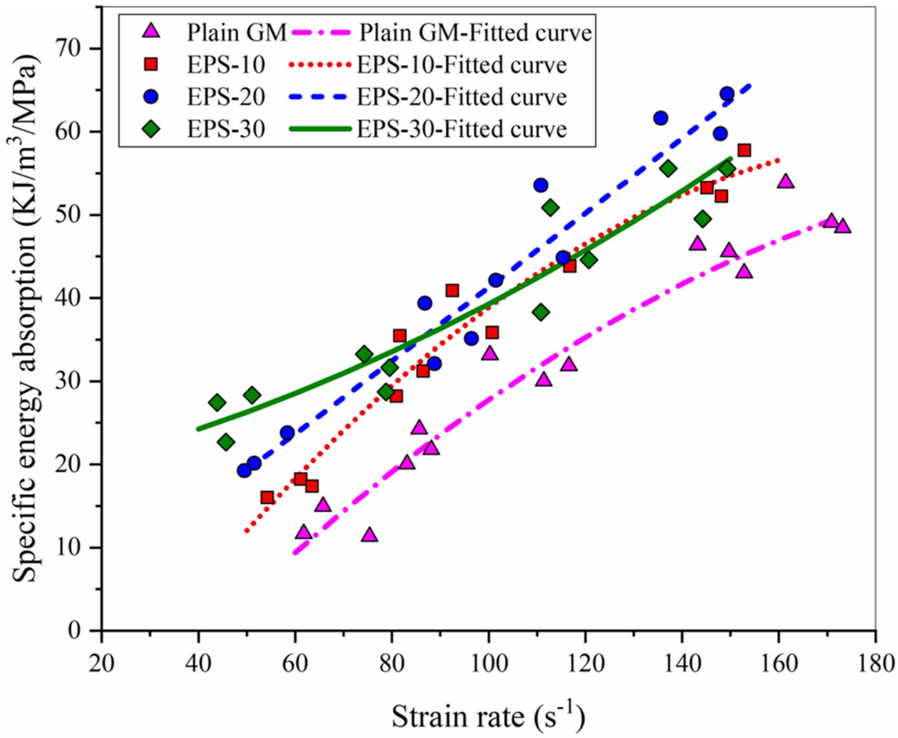

Fig. 17. Comparison of specific energy absorption (SEA) at different strain rates.

Table 4. Summary of dynamic test results for plain GM specimens.

Test No.	Strain rate $\dot{\varepsilon}$ (s^{-1})	Dynamic compressive strength f_{cd} (MPa)	$CDIF_E$	$CDIF_T$	Axial strain ε (%)	$CDIF_\varepsilon$	SED (KJ/m^3)	SEA ($KJ/m^3/MPa$)
Plain-1	61.79	80.20	1.31	1.20	0.37	1.03	711.90	11.65
Plain-2	65.76	82.84	1.35	1.23	0.39	1.08	912.69	14.93
Plain-3	75.36	80.68	1.32	1.20	0.36	1.00	691.21	11.31
Plain-4	83.12	124.91	2.04	1.84	0.39	1.08	1224.82	20.04
Plain-5	85.67	112.33	1.83	1.66	0.4	1.11	1481.85	24.24
Plain-6	88.14	109.81	1.79	1.62	0.39	1.08	1329.71	21.76
Plain-7	100.26	137.20	2.24	2.01	0.41	1.14	2026.15	33.15
Plain-8	111.41	152.19	2.48	2.21	0.44	1.22	1835.16	30.03
Plain-9	116.62	147.99	2.41	2.15	0.43	1.19	1944.55	31.82
Plain-10	143.23	170.13	2.77	2.43	0.47	1.31	2833.90	46.37
Plian-11	152.85	173.29	2.83	2.47	0.51	1.42	2627.84	42.99
Plain-12	149.69	171.01	2.79	2.44	0.46	1.28	2783.44	45.54
Plain-13	161.46	185.24	3.02	2.63	0.48	1.33	3289.27	53.82
Plain-14	170.94	187.21	3.05	2.82	0.49	1.36	3000.42	49.09
Plain-15	173.22	191.02	3.11	2.70	0.45	1.25	2960.42	48.44

Note: $CDIF_E$ is the experimental results of DIF of compressive strength; $CDIF_T$ is the true DIF of compressive strength; $CDIF_\varepsilon$ is the DIF of axial strain at peak stress.

Table 5. Summary of dynamic test results for EPS-10 specimens.

Test No.	Strain rate $\dot{\varepsilon}$ (s^{-1})	Dynamic compressive strength f_{cd} (MPa)	$CDIF_E$	$CDIF_T$	Axial strain ε (%)	$CDIF_\varepsilon$	SED (KJ/m^3)	SEA ($KJ/m^3/MPa$)
EPS-10-1	54.26	49.29	2.03	1.86	0.26	1.04	389.64	16.01
EPS-10-2	61.22	50.56	2.08	1.90	0.29	1.16	443.09	18.21
EPS-10-3	63.54	47.67	1.96	1.80	0.28	1.12	422.61	17.37
EPS-10-4	86.52	65.47	2.69	2.43	0.33	1.32	758.75	31.19
EPS-10-5	80.94	74.00	3.04	2.76	0.31	1.24	685.82	28.19
EPS-10-6	81.68	67.44	2.77	2.51	0.35	1.4	861.86	35.42
EPS-10-7	92.57	75.91	3.12	2.81	0.38	1.52	994.25	40.87

EPS-10-8	116.82	88.04	3.62	3.23	0.43	1.72	1065.27	43.78
EPS-10-9	100.83	83.21	3.42	3.07	0.38	1.52	871.97	35.84
EPS-10-10	145.21	97.22	4.00	3.50	0.45	1.8	1295.25	53.24
EPS-10-11	148.18	98.87	4.06	3.56	0.48	1.92	1270.36	52.21
EPS-10-12	152.92	91.46	3.76	3.28	0.57	2.28	1404.08	57.71

Table 6. Summary of dynamic test results for EPS-20 specimens.

Test No.	Strain rate $\dot{\varepsilon}$ (s^{-1})	Dynamic compressive strength f_{cd} (MPa)	$CDIF_E$	$CDIF_T$	Axial strain ε (%)	$CDIF_\varepsilon$	SED (KJ/m^3)	SEA ($KJ/m^3/MPa$)
EPS-20-1	58.44	38.38	2.35	2.16	0.24	1.09	387.71	23.77
EPS-20-2	51.52	36.05	2.21	2.04	0.26	1.18	328.49	20.14
EPS-20-3	49.53	32.15	1.97	1.82	0.27	1.23	313.69	19.23
EPS-20-4	96.45	55.78	3.42	3.07	0.31	1.41	572.77	35.12
EPS-20-5	88.84	48.00	2.94	2.66	0.32	1.45	523.65	32.11
EPS-20-6	86.82	50.15	3.07	2.78	0.34	1.55	642.11	39.37
EPS-20-7	101.52	62.33	3.82	3.40	0.38	1.73	687.16	42.13
EPS-20-8	110.80	64.40	3.95	3.51	0.36	1.64	873.32	53.55
EPS-20-9	115.45	64.78	3.97	3.53	0.43	1.95	731.47	44.85
EPS-20-10	135.58	64.84	3.98	3.50	0.48	2.18	1005.07	61.62
EPS-20-11	147.95	68.98	4.23	3.70	0.51	2.32	974.25	59.73
EPS-20-12	149.34	71.18	4.36	3.82	0.56	2.55	1052.62	64.54

Table 7. Summary of dynamic test results for EPS-30 specimens.

Test No.	Strain rate $\dot{\varepsilon}$ (s^{-1})	Dynamic compressive strength f_{cd} (MPa)	$CDIF_E$	$CDIF_T$	Axial strain ε (%)	$CDIF_\varepsilon$	SED (KJ/m^3)	SEA ($KJ/m^3/MPa$)
EPS-30-1	51.12	23.37	3.70	3.41	0.17	1.31	179.06	28.33
EPS-30-2	43.87	21.99	3.48	3.22	0.2	1.54	173.31	27.42
EPS-30-3	45.72	23.55	3.73	3.45	0.24	1.85	143.24	22.66
EPS-30-4	78.82	29.20	4.62	4.19	0.29	2.23	181.49	28.72
EPS-30-5	79.54	27.30	4.32	3.92	0.29	2.23	200.01	31.65

EPS-30-6	74.29	26.04	4.12	3.74	0.27	2.08	210.30	33.23
EPS-30-7	110.85	30.75	4.87	4.34	0.33	2.54	241.97	38.29
EPS-30-8	120.75	35.32	5.59	4.96	0.35	2.69	281.70	44.57
EPS-30-9	112.76	32.23	5.10	4.55	0.35	2.69	321.56	50.79
EPS-30-10	137.16	36.02	5.70	5.02	0.4	3.08	351.20	55.57
EPS-30-11	149.33	39.72	6.28	5.50	0.48	3.69	350.95	55.53
EPS-30-12	144.31	37.18	5.88	5.16	0.42	3.23	312.86	49.50

4. Conclusion

This study investigated the dynamic compressive material properties of ambient-cured plain geopolymer mortar (GM) and lightweight geopolymer composites (LGC) with different expanded polystyrene (EPS) volume fractions of 10%, 20%, and 30% by using split Hopkinson pressure bar (SHPB). The failure process and failure mode of plain GM and LGC with various EPS contents were compared. The test results demonstrated the strain rate effect on the compressive strength, axial strain at peak stress and energy absorption within the strain rate range of 43.87 s^{-1} to 173.22 s^{-1}. Based on the findings, the main conclusions can be summarized as follows:

1. The failure process of LGC was different with different EPS contents under high loading rate. The crack initiation time of LGC delayed with the increase of EPS contents under a similar strain rate. The failure patterns of both plain GM and LGC showed strain rate dependence. With the rising strain rate, the number of fragments increased and the average size of fragments reduced.
2. The compressive strength and the corresponding axial strain of plain GM and LGC were strain rate dependent. LGC with more EPS contents was more sensitive to strain rate.

3. The contribution of lateral inertial confinement has been removed to obtain the true dynamic compressive strength. Based on the test results, the empirical formulae for the true dynamic increase factor of compressive strength ($CDIF_T$) of both plain GM and LGC containing different EPS contents were proposed.
4. The energy absorption capacities of plain GM and LGC with EPS became higher with the rising strain rate. The empirical formulae of energy absorption capacities were proposed for plain GM and LGC with various EPS volume fractions. The energy absorption value normalized by the quasi-static compressive strength of LGC was higher than that of plain GM.

Acknowledgements

The authors would like to thank the financial support from the Australian Research Council via Laureate Fellowship FL180100196.

Reference

[1] F.U.A. Shaikh, Mechanical and durability properties of fly ash geopolymer concrete containing recycled coarse aggregates, International Journal of Sustainable Built Environment 5(2) (2016) 277-287.

[2] Y.M. Amran, R. Alyousef, H. Alabduljabbar, M. El-Zeadani, Clean production and properties of geopolymer concrete; A review, Journal of Cleaner Production 251 (2020) 119679.

[3] Z. Li, W. Chen, H. Hao, M.Z.N. Khan, Physical and mechanical properties of new lightweight ambient-cured EPS geopolymer composites, Journal of Materials in Civil Engineering (Accpted 2020).

[4] X. Luo, J. Xu, W. Li, The preparation of energy-absorbing material by using solid waste, RSC Advances 5(12) (2015) 9283-9289.

[5] M.L. Granizo, S. Alonso, M.T. Blanco-Varela, A. Palomo, Alkaline activation of metakaolin: effect of calcium hydroxide in the products of reaction, Journal of the American Ceramic Society 85(1) (2002) 225-231.

[6] C. Cook, FIP manual of lightweight aggregate concrete: Published by The Surrey University Press, Bishopriggs, Glasgow G64 2NZ, Scotland, 1983 ISBN 0 903384 43 4, 259 pp, Elsevier, 1983.

[7] W. Tang, R. Balendran, A. Nadeem, H.Y. Leung, Flexural strengthening of reinforced lightweight polystyrene aggregate concrete beams with near-surface mounted GFRP bars, Building and Environment 41(10) (2006) 1381-1393.

[8] Y. Xu, L. Jiang, J. Xu, Y. Li, Mechanical properties of expanded polystyrene lightweight aggregate concrete and brick, Construction and Building Materials 27(1) (2012) 32-38.

[9] B. Demirel, Optimization of the composite brick composed of expanded polystyrene and pumice blocks, Construction and Building Materials 40 (2013) 306-313.

[10] R.S. Ravindrarajah, A. Tuck, Properties of hardened concrete containing treated expanded polystyrene beads, Cement and Concrete Composites 16(4) (1994) 273-277.

[11] S. Doroudiani, H. Omidian, Environmental, health and safety concerns of decorative mouldings made of expanded polystyrene in buildings, Building and Environment 45(3) (2010) 647-654.

[12] T.K. Yoo, T. Qiu, Optimization of constitutive model parameters for simulation of polystyrene concrete subjected to impact, International Journal of Protective Structures 9(2) (2018) 121-140.

[13] K.G. Babu, D.S. Babu, Behaviour of lightweight expanded polystyrene concrete containing silica fume, Cement and Concrete Research 33(5) (2003) 755-762.

[14] K. Miled, K. Sab, R. Le Roy, Particle size effect on EPS lightweight concrete compressive strength: Experimental investigation and modelling, Mechanics of Materials 39(3) (2007) 222-240.

[15] W. Tang, Y. Lo, A. Nadeem, Mechanical and drying shrinkage properties of structural-graded polystyrene aggregate concrete, Cement and Concrete Composites 30(5) (2008) 403-409.

[16] V. Ferrándiz-Mas, E. García-Alcocel, Durability of expanded polystyrene mortars, Construction and Building Materials 46 (2013) 175-182.

[17] W. Tang, H. Cui, M. Wu, Creep and creep recovery properties of polystyrene aggregate concrete, Construction and Building Materials 51 (2014) 338-343.

[18] Y. Liu, D. Ma, Z. Jiang, F. Xiao, X. Huang, Z. Liu, L. Tang, Dynamic response of expanded polystyrene concrete during low speed impact, Construction and Building Materials 122 (2016) 72-80.

[19] G. Falzone, G.P. Falla, Z. Wei, M. Zhao, A. Kumar, M. Bauchy, N. Neithalath, L. Pilon, G. Sant, The influences of soft and stiff inclusions on the mechanical properties of cementitious composites, Cement and Concrete Composites 71 (2016) 153-165.

[20] E.L. Bai, J.Y. Xu, Z.G. Gao, Study on Deformation Property of EPS Concrete under Impact Loading, Applied Mechanics and Materials, Trans Tech Publ, 2011, pp. 809-814.

[21] S. Lu, J. Xu, E. Bai, X. Luo, Effect of particles with different mechanical properties on the energy dissipation properties of concrete, Construction and Building Materials 144 (2017) 502-515.

[22] E.L. Bai, J.Y. Xu, S. Lu, K.X. Lin, Y.M. Zhang, Comparative study on the dynamic properties of lightweight porous concrete, RSC advances 8(26) (2018) 14454-14461.

[23] H.J. Mohammed, M. Zain, Experimental application of EPS concrete in the new prototype design of the concrete barrier, Construction and Building Materials 124 (2016) 312-342.

[24] C. Atiş, E. Görür, O. Karahan, C. Bilim, S. İlkentapar, E. Luga, Very high strength (120 MPa) class F fly ash geopolymer mortar activated at different NaOH amount, heat curing temperature and heat curing duration, Construction and Building Materials 96 (2015) 673-678.

[25] J.L. Provis, J.S.J. Van Deventer, Geopolymers: structures, processing, properties and industrial applications, Elsevier2009.

[26] M. Nasvi, T. Rathnaweera, E. Padmanabhan, Geopolymer as well cement and its mechanical integrity under deep down-hole stress conditions: application for carbon capture and storage wells, Geomechanics and Geophysics for Geo-Energy and Geo-Resources 2(4) (2016) 245-256.

[27] Y. Hu, Z. Tang, W. Li, Y. Li, V.W. Tam, Physical-mechanical properties of fly ash/GGBFS geopolymer composites with recycled aggregates, Construction and Building Materials 226 (2019) 139-151.

[28] B. Singh, G. Ishwarya, M. Gupta, S. Bhattacharyya, Geopolymer concrete: A review of some recent developments, Construction and Building Materials 85 (2015) 78-90.

[29] P. Posi, C. Ridtirud, C. Ekvong, D. Chammanee, K. Janthowong, P. Chindaprasirt, Properties of lightweight high calcium fly ash geopolymer concretes containing recycled packaging foam, Construction and Building Materials 94 (2015) 408-413.

[30] F. Colangelo, G. Roviello, L. Ricciotti, V. Ferrandiz-Mas, F. Messina, C. Ferone, O. Tarallo, R. Cioffi, C. Cheeseman, Mechanical and thermal properties of lightweight geopolymer composites, Cement and Concrete Composites 86 (2018) 266-272.

[31] G. Kakali, D. Kioupis, A. Skaropoulou, S. Tsivilis, Lightweight geopolymer composites as structural elements with improved insulation capacity, MATEC Web of Conferences, EDP Sciences, 2018.

[32] F. Aslani, A. Deghani, Z. Asif, Development of Lightweight Rubberized Geopolymer Concrete by Using Polystyrene and Recycled Crumb-Rubber Aggregates, Journal of Materials in Civil Engineering 32(2) (2020) 04019345.

[33] ASTM, Standard Specification for Coal Fly Ash and Raw or Calcined Natural Pozzolan for Use in Concrete, ASTM C618-19 (2019).

[34] P. Nath, P.K. Sarker, Effect of GGBFS on setting, workability and early strength properties of fly ash geopolymer concrete cured in ambient condition, Construction and Building Materials 66 (2014) 163-171.

[35] ASTM, Standard Test Method for Density and Void Content of Freshly Mixed Pervious Concrete, ASTM C1688-14 (2014).

[36] ASTM, Standard Test Method for Compressive Strength of Cylindrical Concrete Specimens, ASTM C39-18 (2018).

[37] ASTM, Standard Test Method for Static Modulus of Elasticity and Poisson's Ratio of Concrete in Compression, ASTM C469-14 (2014).

[38] T. Lv, X. Chen, G. Chen, Analysis on the waveform features of the split Hopkinson pressure bar tests of plain concrete specimen, International Journal of Impact Engineering 103 (2017) 107-123.

[39] U. Lindholm, Some experiments with the split hopkinson pressure bar∗, Journal of the Mechanics and Physics of Solids 12(5) (1964) 317-335.
[40] D. Grote, S. Park, M. Zhou, Dynamic behavior of concrete at high strain rates and pressures: I. experimental characterization, International Journal of Impact Engineering 25(9) (2001) 869-886.
[41] J. Guo, Q. Chen, W. Chen, J. Cai, Tests and Numerical Studies on Strain-Rate Effect on Compressive Strength of Recycled Aggregate Concrete, Journal of Materials in Civil Engineering 31(11) (2019) 04019281.
[42] M. Zhang, H. Wu, Q. Li, F. Huang, Further investigation on the dynamic compressive strength enhancement of concrete-like materials based on split Hopkinson pressure bar tests. Part I: Experiments, International Journal of Impact Engineering 36(12) (2009) 1327-1334.
[43] Y. Hao, H. Hao, Dynamic compressive behaviour of spiral steel fibre reinforced concrete in split Hopkinson pressure bar tests, Construction and Building Materials 48 (2013) 521-532.
[44] C. Wang, W. Chen, H. Hao, S. Zhang, R. Song, X. Wang, Experimental investigations of dynamic compressive properties of roller compacted concrete (RCC), Construction and Building Materials 168 (2018) 671-682.
[45] C. Zhai, L. Chen, Q. Fang, W. Chen, X. Jiang, Experimental study of strain rate effects on normal weight concrete after exposure to elevated temperature, Materials and Structures 50(1) (2017) 40.
[46] T.M. Pham, W. Chen, A.M. Khan, H. Hao, M. Elchalakani, T.M. Tran, Dynamic compressive properties of lightweight rubberized concrete, Construction and Building Materials 238 (2020) 117705.
[47] Z. Yin, W. Chen, H. Hao, J. Chang, G. Zhao, Z. Chen, K. Peng, Dynamic compressive test of gas-containing coal using a modified split hopkinson pressure bar system, Rock Mechanics and Rock Engineering 53(2) (2020) 815-829.
[48] M.Z.N. Khan, Y. Hao, H. Hao, F.U.A. Shaikh, Experimental evaluation of quasi-static and dynamic compressive properties of ambient-cured high-strength plain and fiber reinforced geopolymer composites, Construction and Building Materials 166 (2018) 482-499.
[49] Y. Hao, H. Hao, G. Jiang, Y. Zhou, Experimental confirmation of some factors influencing dynamic concrete compressive strengths in high-speed impact tests, Cement and Concrete Research 52 (2013) 63-70.
[50] Y. Hao, H. Hao, Z.-X. Li, Numerical analysis of lateral inertial confinement effects on impact test of concrete compressive material properties, International Journal of Protective Structures 1(1) (2010) 145-167.
[51] K.N. Feng, D. Ruan, Z. Pan, F. Collins, Y. Bai, C.M. Wang, W.H. Duan, Mechanical behavior of geopolymer concrete subjected to high strain rate compressive loadings, Materials and Structures 48(3) (2015) 671-681.
[52] G. Ding, J. Xu, Z. Hu, F. Xi, E. Bai, Mechanical properties of early-strengthened polystyrene concrete under impact load, Journal of Vibration and Shock 30(3) (2011) 269-273.
[53] J. Xie, O. Kayali, Effect of initial water content and curing moisture conditions on the development of fly ash-based geopolymers in heat and ambient temperature, Construction and Building Materials 67 (2014) 20-28.
[54] S. Harsh, Z. Shen, D. Darwin, Rate sensitive behavior of cement paste and mortar in compression, University of Kansas Center for Research, Inc., 1989.
[55] X.X. Zhang, C.Y. Rena, G. Ruiz, M. Tarifa, M.A. Camara, Effect of loading rate on crack velocities in HSC, International Journal of Impact Engineering 37(4) (2010) 359-370.
[56] L.L. Wang, F.H. Zhou, Z.J. Sun, Y.Z. Wang, S.Q. Shi, Studies on rate-dependent macro-damage evolution of materials at high strain rates, International Journal of Damage Mechanics 19(7) (2010) 805-820.